

PAPER

Magnetic phase diagram of the olivine-type Mn_2GeO_4 single crystal estimated from magnetic, resonance and thermodynamic properties

To cite this article: N V Volkov *et al* 2013 *J. Phys.: Condens. Matter* **25** 136003

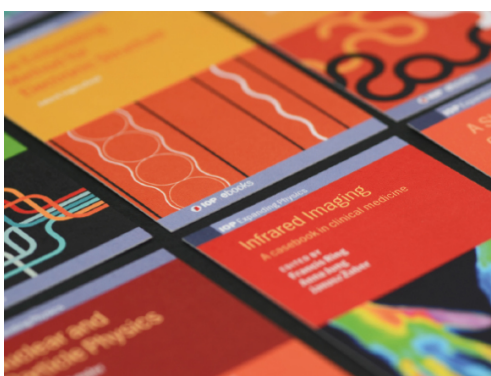
View the [article online](#) for updates and enhancements.

Related content

- [Magnetic and specific heat properties of \$\text{YFe}_3\(\text{BO}_3\)_4\$ and \$\text{ErFe}_3\(\text{BO}_3\)_4\$](#)
E A Popova, A N Vasiliev, V L Temerov *et al.*
- [Irreversible field-induced magnetic phase transitions and properties of \$\text{Ho}_3\text{Co}\$](#)
N V Baranov, T Goto, G Hilscher *et al.*
- [Synthesis and magnetic properties of a new series of triangular-lattice magnets, \$\text{Na}_2\text{BaMV}_2\text{O}_8\$ \(M = Ni, Co, and Mn\)](#)
Genki Nakayama, Shigeo Hara, Hirohiko Sato *et al.*

Recent citations

- [Stress-induced magnetic domain selection reveals a conical ground state for the multiferroic phase of \$\text{Mn}_2\text{GeO}_4\$](#)
J. S. White *et al*
- [High pressure and multiferroics materials: a happy marriage](#)
Edmondo Gilioli and Lars Ehm



IOP | ebooks™

Bringing together innovative digital publishing with leading authors from the global scientific community.

Start exploring the collection—download the first chapter of every title for free.

Magnetic phase diagram of the olivine-type Mn_2GeO_4 single crystal estimated from magnetic, resonance and thermodynamic properties

N V Volkov^{1,2}, N V Mikhashenok¹, K A Sablina¹, O A Bayukov¹,
M V Gorev¹, A D Balaev¹, A I Pankrats^{1,2}, V I Tugarinov¹,
D A Velikanov^{1,2}, M S Molochev¹ and S I Popkov¹

¹ Kirensky Institute of Physics SB RAS, 660036 Krasnoyarsk, Russia

² Siberian Federal University, Department of Physics, 660041 Krasnoyarsk, Russia

E-mail: natali_sapronova@mail.ru

Received 30 October 2012, in final form 21 January 2013

Published 5 March 2013

Online at stacks.iop.org/JPhysCM/25/136003

Abstract

Mn_2GeO_4 single crystals with the olivine structure grown by the modified flux method have been investigated. Pronounced magnetic phase transitions at $T_1 = 47.7$ K, $T_2 = 17$ K and $T_3 = 5.5$ K, with T_2 being dependent on an applied magnetic field, have been found. Based on the data of magnetic, resonance and temperature measurements, the entire phase diagram of Mn_2GeO_4 has been built. Mn_2GeO_4 is shown to be a material with a complex magnetic structure consisting of two magnetic subsystems.

(Some figures may appear in colour only in the online journal)

1. Introduction

The wide variety of natural minerals with diverse crystal structures determining their intriguing physical properties have been an inexhaustible source of objects for study in the physics of condensed matter and magnetic phenomena.

Unfortunately, natural minerals, with rare exceptions, are contaminated with various impurities nonuniformly distributed both inside a sample and from one sample to another. This fact complicates investigations of the impurity-sensitive physical properties of natural materials. The search for magnetically unexplored minerals for reproduction under laboratory conditions involves, along with the study of their crystallographic peculiarities, the estimation of possible synthesis routes for pure single crystals, this being the most informative form for investigations of the magnetic properties of the chosen compounds.

Silicates are the most widely occurring minerals, taking into account their fraction in the Earth's crust. Their diverse structures are caused by the variety of ways interconnections

can form between the silicon–oxygen tetrahedra and triangles. In the presence of magnetic ions, the varying nature of the silicon–oxygen cores plays a decisive role in the formation of a range of magnetic structures in silicate minerals: chains, ribbons, multilayers, etc.

The fabrication of artificial silicate oxide compounds under laboratory conditions is complicated by the high melting temperatures of these materials. The isomorphism of Si^{4+} and Ge^{4+} in the crystals [1] makes it possible to study the physical properties of silicate minerals in the isostructural and isomorphous germanates. As an analog of enstatite MnSiO_3 , we grew MnGeO_3 single crystals with the pyroxene structure and investigated their magnetic properties [2, 3]. On the basis of minerals of the pyroxene group with the general formula AMSi_2O_6 and the chain magnetic structure, the isomorphous AMGe_2O_6 ($A = \text{Li, K, Na, \dots}$ and $M = \text{Fe}^{2+}, \text{Mn}^{2+}$) analogs have been studied [4, 5]. Another example is the $\text{Pb}_2\text{Fe}_2\text{Ge}_2\text{O}_9$ single crystal grown by us as an analog of $\text{Pb}_2\text{Fe}_2\text{Si}_2\text{O}_9$ [6].

When preparing our work on the magnetic properties and specific heat of Mn_2GeO_4 single crystals recently investigated by us, we found that study [7] demonstrated that this compound has been attracting the attention of researchers due to its multicritical properties and the suggested polarized state, which stimulated our investigations of the magnetic characteristics of Mn_2GeO_4 single crystals [8]. In addition, we believe that studying the temperature and field dependences of magnetization, specific heat and resonance properties and the estimation of exchange interactions will be useful in clarifying the change of magnetic ordering in Mn_2GeO_4 in the temperature range 2–300 K. Furthermore, we got the opportunity to compare our conclusions on the nature of magnetic transitions with the neutron-diffraction data reported in the mentioned study.

Here, we describe the method used to fabricate the Mn_2GeO_4 crystals, identify their structure, and present results of measurements of their magnetic properties in a magnetic field oriented along the three principal crystallographic directions at temperatures from 2 to 300 K in magnetic fields up to 80 kOe. In addition, we performed calorimetric measurements in the same temperature range.

2. Experimental details

Mn_2GeO_4 single crystals were grown by the flux method using the technique that was applied for growing these crystals for the first time [2]. High-quality MnO and GeO_2 in the stoichiometric ratio were taken as initial components and MnCl_2 was used as a solvent. The single crystals had typical dimensions of $0.5 \times 1 \times 3 \text{ mm}^3$.

The crystal structure of Mn_2GeO_4 was determined with a SMART APEX (Bruker AXS) autodiffractometer for single crystals. The model fitting was made by direct methods using the SHELXS program [9]. The coordinates of all atoms were determined. X-ray patterns were obtained at room temperature. The directions of the crystallographic axes in the measured sample were determined with a D8-ADVANCE powder x-ray diffractometer.

Magnetic measurements were performed on a Magnetic Property Measurement System (Quantum Design, USA) in the temperature range 2–300 K and magnetic fields up to 50 kOe and with a vibrating sample magnetometer of original construction in the temperature range 4.2–300 K in magnetic fields up to 80 kOe at different orientations of the magnetic field relative to the principal axes.

The specific heat of Mn_2GeO_4 was measured using a special option of a Physical Property Measurement System (Quantum Design, USA) by a relaxation technique. The data were obtained at temperatures from 2 to 300 K in magnetic fields up to 90 kOe. The absolute accuracy of the method was no worse than 1% over the entire temperature range.

The resonance measurements were performed with a magnetic resonance spectrometer [10] at frequencies of 25–140 GHz in magnetic fields up to 80 kOe.

Table 1. The main crystallographic data and experimental parameters.

Crystallographic data	
Chemical formula	Mn_2GeO_4
Space group, Z	$Pnma$, 4
a , (Å)	10.740(2)
b , (Å)	6.312(1)
c , (Å)	5.077(1)
V , (Å ³)	344.17(6)
Data collection parameters	
Wavelength	Mo $K\alpha$, $\lambda = 0.7106 \text{ Å}$
R_{int}	0.039
$2\theta_{\text{max}}$ (deg)	59.10
h	−14 → 14
k	−8 → 8
l	−6 → 6
Refining results	
$R[F^2 > 2\sigma(F^2)]$	0.0226
$wR(F^2)$	0.0595

3. Results and discussion

3.1. Crystal structure

The main crystallographic characteristics and parameters of the x-ray experiment are given in table 1. The crystal structure is identical to the previously reported structure of Mn_2GeO_4 [11].

Some important aspects of the olivine structure necessary for understanding the magnetic structure of Mn_2GeO_4 are summarized below. The Mn_2GeO_4 crystal structure can be identified as an arrangement of MnO_6 octahedra in layers perpendicular to the c axis at $z = 0$ and 0.5 (figure 1). There are two positions of manganese ions: Mn1 is located in the center of symmetry (4a), and Mn2 is in the mirror plane (4c) (figure 1(a)). Mn1 cations are located exactly in the layers, while Mn2 cations are slightly shifted along the c axis. The Mn1O_6 octahedra have common edges and form single chains along the b axis. The Mn2O_6 octahedra are attached on alternate sides to the Mn1O_6 chains in a way such that the whole arrangement of Mn1O_6 and Mn2O_6 octahedra forms zigzag chains along the b axis (figure 1(b)). Germanium ions are coordinated by four oxygen ions, forming isolated GeO_4 tetrahedra connected by divalent Mn cations.

3.2. Static magnetic properties

Figure 2 shows the temperature dependences of inverse susceptibility $1/\chi$ of the Mn_2GeO_4 single crystal in an applied magnetic field $H = 1 \text{ kOe}$. There are three pronounced anomalies along the c axis at $T_1 = 47.7 \text{ K}$, $T_2 = 17.2 \text{ K}$ and $T_3 = 5.5 \text{ K}$, which correspond to the magnetic phase transitions. The measurements were performed on two single-crystal samples with the exact orientation of the magnetic field along the a , b and c crystallographic axes. The results of the two experiments are identical. The

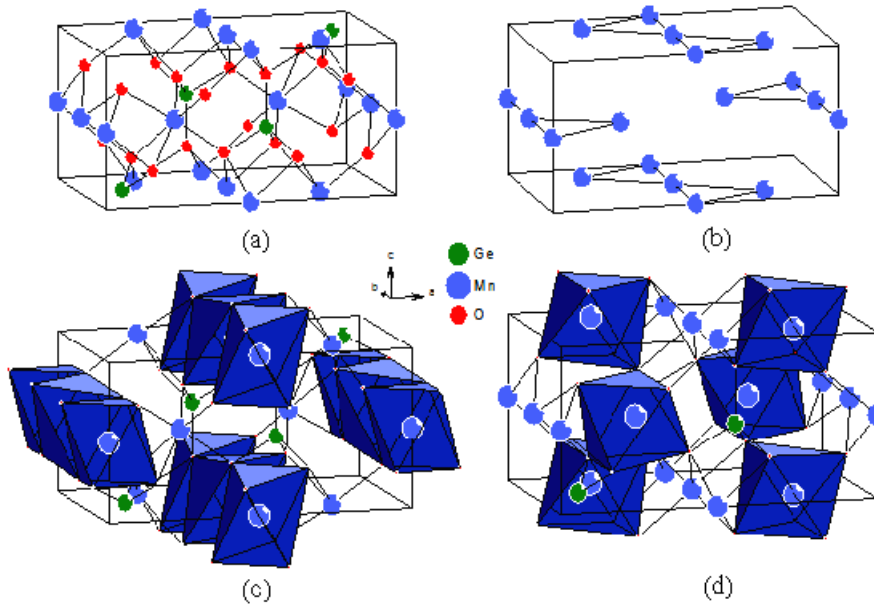


Figure 1. Crystal structure of Mn_2GeO_4 olivine: (a) unit cell, (b) frame of magnetic ions, (c) frame of edge-sharing Mn1 octahedra, and (d) frame of corner-sharing Mn2 octahedra.

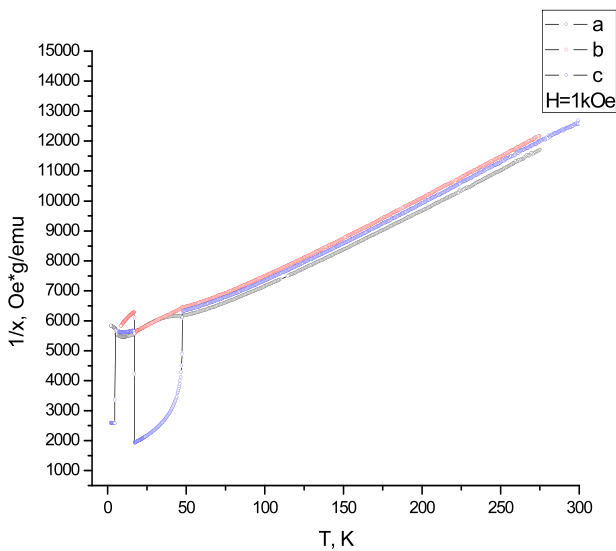


Figure 2. Temperature dependences of inverse susceptibility of Mn_2GeO_4 in a field of 1 kOe for the three crystallographic directions.

magnetization (susceptibility) was determined in magnetic fields from 20 to 50 kOe at temperatures of 2–300 K. It should be noted that for all the three directions the linear portions in the dependences $1/\chi(T)$, where the Curie–Weiss law is valid, start above 150 K, indicating the paramagnetic state.

Deviation from the Curie–Weiss law with decreasing temperature is caused, most likely, by the occurrence of the short-range ordering and is typical of most antiferromagnets. Susceptibility depends on the direction of the applied magnetic field over the entire temperature range. This is the unambiguous evidence for the anisotropy of the magnetic properties, including the paramagnetic region. In the latter,

Table 2. Curie–Weiss temperatures Θ_{CW} , Curie constants C_{CW} and effective magnetic moments μ_{eff} determined from the Curie–Weiss fits of high-temperature portions of magnetic susceptibility of Mn_2GeO_4 .

	C_{CW} (g K emu ⁻¹)	Θ_{CW} (K)	μ_{eff} (μ_{B})
<i>a</i>	37.2	−161	6.06
<i>b</i>	36	−166	5.95
<i>c</i>	36.5	−164	6.02

however, the value of the anisotropy is insignificant as compared with that in Fe_2SiO_4 [12] or Co_2SiO_4 [13].

Effective magnetic moments μ_{eff} , Curie constants C_{CW} and Curie–Weiss temperatures Θ_{CW} calculated using the Curie–Weiss law are given in table 2. It can be seen that the experimental values of the effective moment coincide well with the theoretical value $5.92 \mu_{\text{B}}$ for Mn^{2+} ($s = 5/2$). Negative values of Θ_{CW} indicate the predominance of the antiferromagnetic interactions in this compound.

Now, let us consider the temperature dependence of magnetization below 50 K for the grown Mn_2GeO_4 single crystals. This dependence was obtained in different magnetic fields for the three crystallographic directions. The magnetic transitions, especially those at T_2 and T_3 , occur in the narrow temperature intervals $\Delta T \sim 1.0$ K. Temperature dependences of magnetization in fields of 20 Oe, 1 kOe and 50 kOe are presented in figure 3. Impressive is the dependence along the *c* direction. The behavior of magnetization below T_1 , using the value $\Theta_{\text{CW}} \sim -160$ K, is typical of antiferromagnets with a canted structure that leads to the occurrence of weak ferromagnetism along the *c* axis at $T_1 = T_{\text{N}}$. For the *a* and *b* axes, one can see only a minor variation in magnetization in the temperature range T_1 – T_2 . This is possibly related to inexact orientation of the magnetic field along these axes.

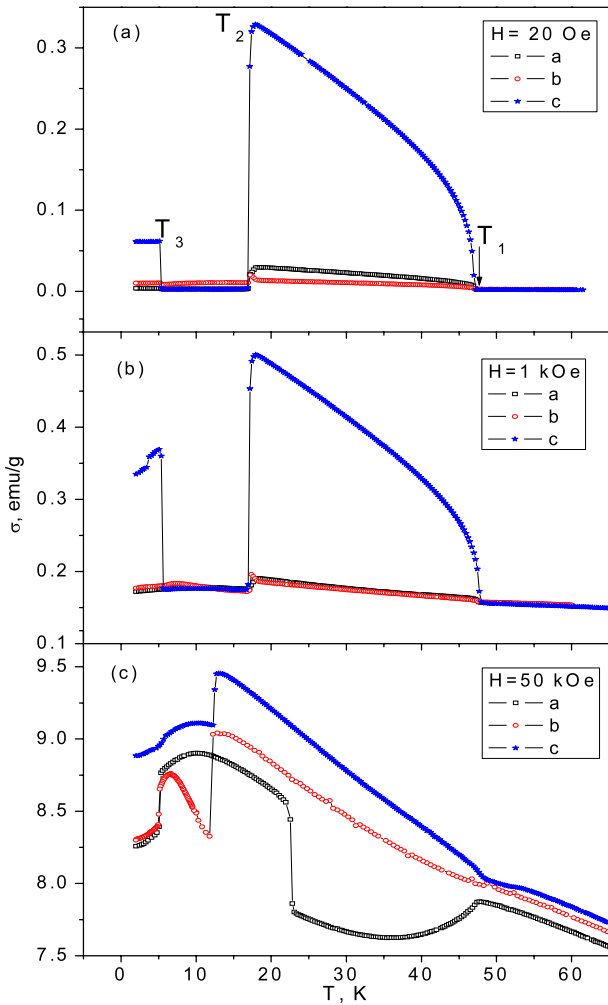


Figure 3. Temperature dependence of magnetization of Mn_2GeO_4 for the principal crystallographic directions in different magnetic fields.

As the magnetic field is increased, the magnetization along the c axis grows and generally retains its characteristic behavior (figure 3(b)). However, in the field $H = 1$ kOe, the magnetization at temperatures below T_3 starts decreasing, unlike the case of $H = 20$ Oe, where it remains invariable up to 2 K. While transition temperatures T_1 and T_3 are nearly independent of the applied magnetic field, temperature T_2 , at which magnetization sharply drops, depends on the field, specifically, decreasing from 17.2 K at $H = 20$ Oe to 12.6 K at $H = 50$ kOe (figure 3), which is consistent with the data reported in [7] and results of the specific heat measurements presented below.

As the field is further increased to 50 kOe, the temperature dependences of magnetization significantly change for all the three directions. The strongest change is observed at $H \parallel a$ below T_1 . At T_1 , there is a cusp-like susceptibility anomaly, characteristic of the case when the magnetic field is oriented along the easy axis of the antiferromagnet (figure 3(c)). With a further decrease in temperature, the differences are also observed.

Field dependences of magnetization for all the crystallographic directions of the single crystal were measured

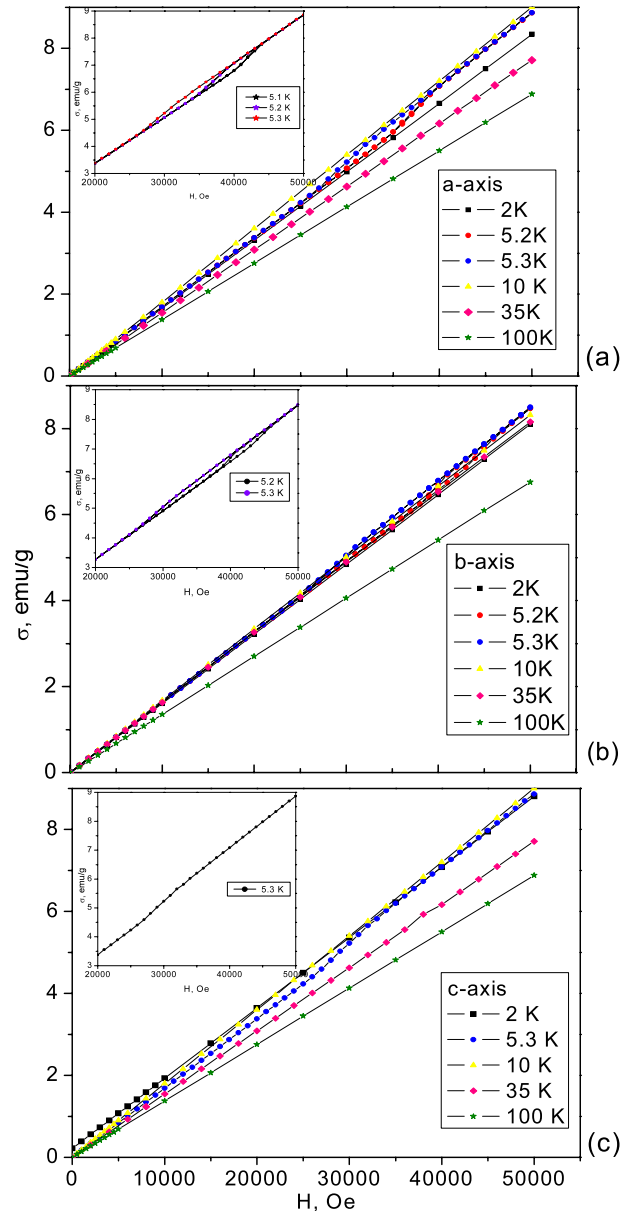


Figure 4. Field dependences of magnetization for the three crystallographic directions in the Mn_2GeO_4 crystal at different temperatures and magnetic field orientations (a) $H \parallel a$, (b) $H \parallel b$ and (c) $H \parallel c$. The insets show stepless anomalies.

in fields up to 80 kOe at temperatures from 2 to 100 K. These dependences are presented in figure 4 for the a , b and c directions in the crystal in fields up to 50 kOe. The dependences are generally identical and linear. However, in the temperature region $T < T_3$, there are stepless deviations from the linear behavior (insets in figure 4).

In addition, we measured field dependences of magnetization along the principal crystallographic directions in fields up to 80 kOe in the temperature intervals where the magnetic phase transitions are observed (figure 5).

Let us consider the field dependence for the a direction in the range from 17 K to the Neel temperature (figure 5(a)). One can see the magnetization jump at a certain value of the applied magnetic field H_c , above and below which there

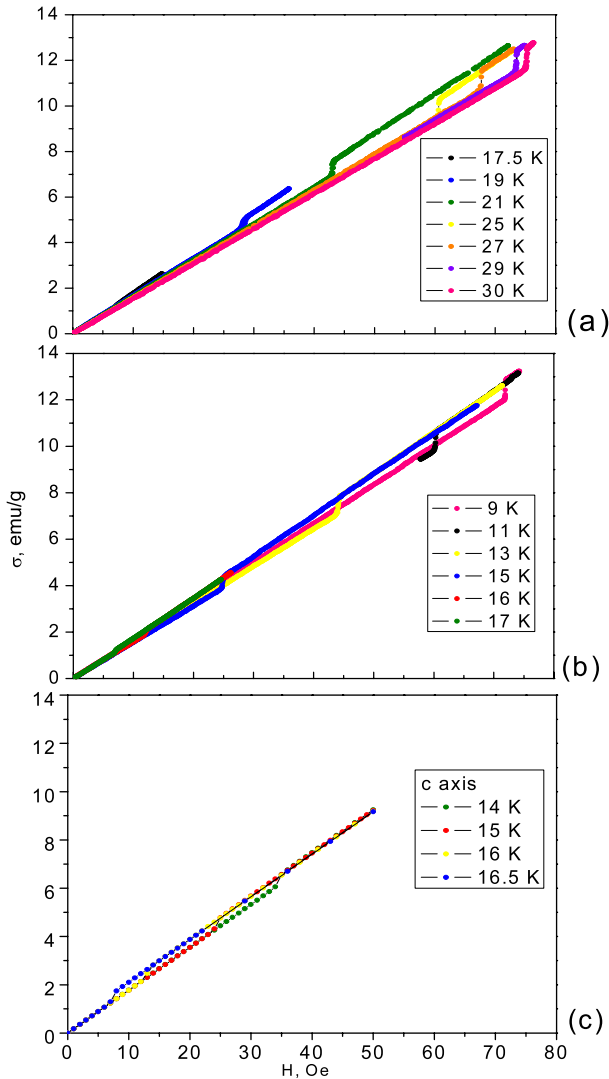


Figure 5. Magnetic field dependences of magnetization for Mn_2GeO_4 at (a) $H \parallel a$, (b) $H \parallel b$ and (c) $H \parallel c$.

are linear portions starting at the origin of coordinates. Such a behavior is typical of the spin-reorientation (spin-flop) transition. The critical field H_{ca} of this transition decreases with a temperature decrease from T_N , and at $T = T_2$ vanishes. In our opinion, the magnetization jump is caused by the transition from χ_{\parallel} at $H < H_c$ to χ_{\perp} at $H > H_c$, with the inequality $\chi_{\parallel} < \chi_{\perp}$ always being valid. It means that in the absence of a magnetic field, the magnetic structure of the crystal in the temperature range $T_2 - T_N$ is antiferromagnetically ordered and the antiferromagnetic axis is parallel to the a axis.

In the b axis direction, the field dependences in the range $T_3 - T_2$ behave similarly (figure 5(b)), but the critical field H_{cb} decreases with increasing temperature and also vanishes at $T = T_2$. Thus, having analyzed the field dependences for these two directions, we suggest that in the temperature range $T_3 - T_2$ the antiferromagnetic axis is directed along the b axis and T_2 is the temperature of the spontaneous transition between these two states.

When the magnetic field is directed along the c axis, there are also magnetization jumps in the temperature region $T_3 - T_2$ and the critical field H_{cc} depends on temperature, similar to the case of the b direction. However, unlike the two other directions, the phase transition is not accompanied by a change in the field dependence slope. This feature is apparently explained by the fact that both the portions of the field dependence are characterized by the perpendicular susceptibility, i.e., during this transition the vector of antiferromagnetism \mathbf{L} rotates in the plane perpendicular to the c axis. In other words, the magnetic field $H \parallel c$ also induces a spin-reorientation transition between the states with $\mathbf{L} \parallel b$ and $\mathbf{L} \parallel a$. The magnetization jump is caused by the occurrence of a weak ferromagnetic moment in the field-induced phase at $H > H_{cc}$. Consequently, in this crystal the weak ferromagnetic moment is present at $\mathbf{L} \parallel a$ and absent at $\mathbf{L} \parallel b$.

Note the important feature in the temperature dependences of the critical fields for the transition between the states with $\mathbf{L} \parallel b$ and $\mathbf{L} \parallel a$. For all the orientations of the magnetic field, the critical fields H_c tend to zero on approaching T_2 . At the same time, the temperature dependence behaves differently at different magnetic field orientations. If the magnetic field is oriented along the rhombic a axis, then the critical field increases on heating the crystal. Such a behavior is typical of the spin-flop transitions and caused by the fact that the difference $\chi_{\perp} - \chi_{\parallel}$ that determines the value of the critical field decreases on approaching T_N . At the same time, for the two other directions, the temperature dependence is the reverse. These features can be qualitatively explained by the fact that the magnetic anisotropy that determines the orientation of the antiferromagnetic vector in this crystal comprises several contributions that have opposite signs and, consequently, partially compensate each other. These can be, for example, the magnetically anisotropic contributions from the subsystems of edge-sharing Mn1 and corner-sharing Mn2 octahedra. Due to the difference between the temperature dependences of the contributions, the resulting magnetic anisotropy constant changes its sign at the temperature T_2 , which leads to the spontaneous orientation transition. One of the contributions apparently depends on the magnetic field applied in different crystallographic directions, which can cause field-induced orientation transitions in the temperature range $T_3 - T_2$.

Similar temperature dependences of the critical fields caused by the competition of the magnetically anisotropic contributions of the magnetic subsystems of Fe^{3+} and rare-earth ions were observed for the magnetic phase diagrams of rare-earth ferrobates $\text{GdFe}_3(\text{BO}_3)_4$ and $\text{HoFe}_3(\text{BO}_3)_4$ [14, 15].

We would like to emphasize an intriguing feature in the field dependences of magnetization for the a and b axes. Surprising is the small value of the magnetization jump at H_{ca} and H_{cb} , which is atypical of the ordinary two-sublattice antiferromagnets, for example, MnGeO_3 , in which the classical spin-flop transition is observed [3]. The magnetization can behave in this way when the field dependence is the superposition of two different dependences. This suggests the existence of two magnetic subsystems in

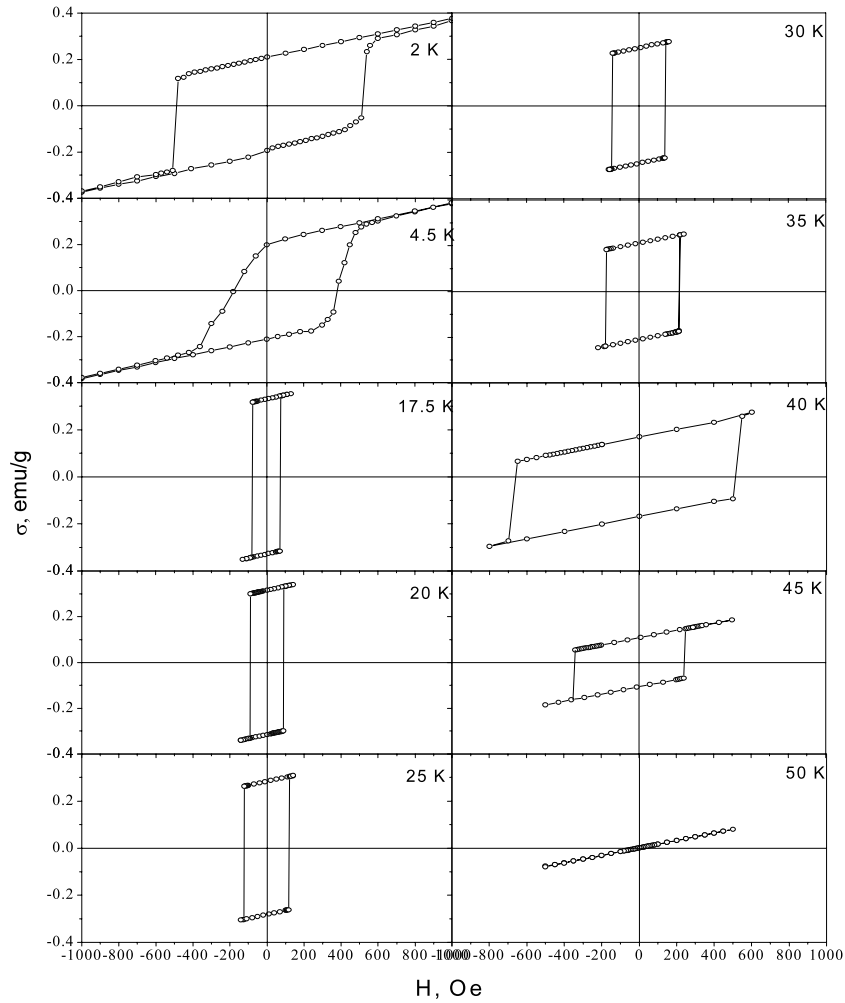


Figure 6. Hysteresis loops for Mn_2GeO_4 in the magnetic field applied along the c axis.

Mn_2GeO_4 . Below we show that Mn_2GeO_4 can be considered as a two-subsystem magnet with one of the subsystems being formed by Mn1 and the other by Mn2 ions.

In the temperature regions T_1 – T_2 and below T_3 , there are hysteresis loops of different shapes only along the c axis (figure 6). It can be seen that the hysteresis loops obtained at temperatures of 35, 40 and 45 K are shifted relative to the axis $H = 0$. The weak remanent magnetization in the c direction in the temperature range T_1 – T_2 indicates weak ferromagnetism caused by the canted magnetic structure. If we put the values of the remanent magnetization obtained from the hysteresis loops in this temperature region on the temperature dependence of magnetization along the c axis (figure 3(a)), they, as expected, will fit this curve well. In the temperature region below T_3 , the hysteresis loops are irregular. Below we show that the remanent magnetization in this region is caused by a more complex magnetic structure.

3.3. Specific heat study

We investigated the thermodynamic properties of our Mn_2GeO_4 samples. The obtained Mn_2GeO_4 specific heat

data as a function of temperature are plotted in figures 7(a) and (b). The dependence $C_p(T)$ demonstrates the classical picture of the λ -type transition around $T_N = 47$ K: with increasing temperature, the specific heat gradually rises on the low-temperature side of the transition and continuously decreases above the Neel temperature, implying a substantial contribution of critical fluctuations (figure 7(a)). Moreover, there are two narrow anomalies at T_2 and T_3 , typical of the first-order phase transitions. All the three anomalies in $C_p(T)$ correlate with the magnetic phase transitions (figure 4). Temperature T_2 is extremely sensitive to the applied magnetic field (inset in figure 7(a)) and decreases from 17.1 K at $H = 0$ T to 5.7 K at $H = 9$ T. An additional shoulder-like anomaly of specific heat near 7 K is observed (figure 7(a)). In figure 7(b), our results are presented together with the literature data on specific heat for other olivines. It should be noted that the phase transitions similar to the transitions of Mn_2GeO_4 at T_2 and T_3 for other olivines have not so far been observed. However, the measurements of specific heat of Mn_2SiO_4 [16] and Fe_2SiO_4 [17] yielded small ‘shoulders’ near 12 and 20 K, respectively.

The authors of [16] attributed the shoulder anomaly C_p of Mn_2SiO_4 to the magnetic phase transition from the

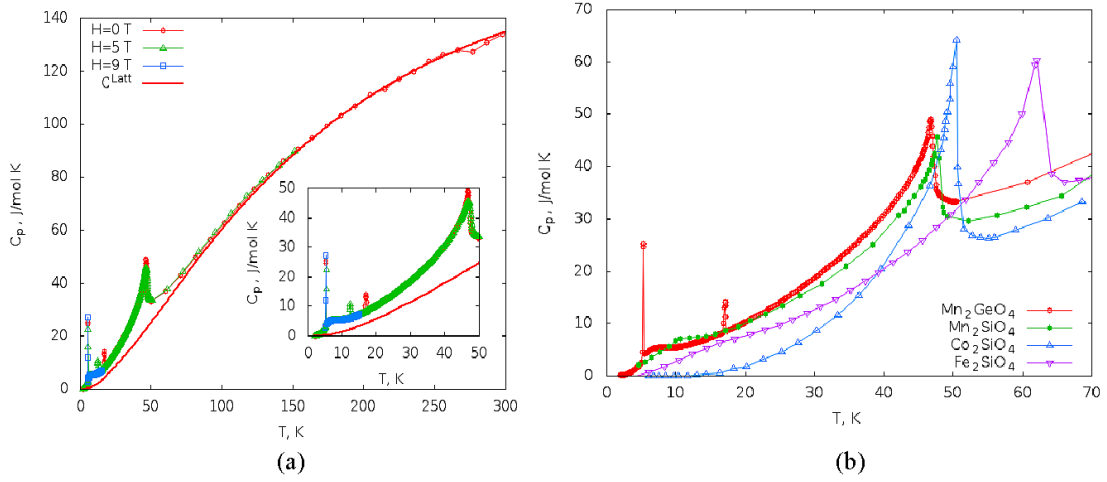


Figure 7. (a) Temperature dependence of the specific heat of Mn_2GeO_4 . The inset shows the effect of a magnetic field on the position of the T_2 maximum. (b) Temperature dependences of the specific heat for olivines.

collinear to canted spin structure, while in [17] the similar anomaly in C_p for Fe_2SiO_4 is explained differently. The authors of [17] suggested that the ‘shoulder’ is related to the Schottky contribution to specific heat near 20 K arising from the thermal population of the lowest-lying excited states in the crystal-field-split manifold of the M1 site due to the spin–orbit coupling. This explanation of the ‘shoulder’ works in the case of Mn_2GeO_4 , considering that Mn1 ions (Mn1 subsystem) appear in the specific heat as the Schottky anomaly and Mn2 ions (Mn2 subsystem) are responsible for the λ -anomaly at T_N .

To make sure that the assumption on partial participation of Mn ions in the formation of the magnetic order at T_N is correct, we estimate separate contributions to the specific heat of Mn_2GeO_4 .

The specific heat of a crystalline solid involves several contributions:

$$C_v = C_v^{\text{latt}} + C_v^{\text{Sch}} + C_v^{\text{mag}} \quad (1)$$

where C_v^{latt} is the lattice vibration contribution, C_v^{Sch} is the Schottky contribution and C_v^{mag} is the magnetic contribution. The contributions of free electrons, crystal defects and anharmonic effects are small and can be neglected. The small difference between C_v and C_p can be evaluated by the thermodynamic relationship, which requires information on the coefficient of thermal expansion, the volume of the material, and isothermal compressibility. It was shown, however, [18, 19] that the difference between C_v and C_p is important only at high temperatures.

To estimate the lattice contribution, we used the results of the first-principles calculations of phonon density of states $g(\omega)$ in the framework of the Gordon–Kim rigid ion model [20] (figure 8).

The lattice contribution to the specific heat given by the equation

$$C_v^{\text{latt}} = nk_B \int_0^\infty \left(\frac{\hbar\omega}{k_B T} \right)^2 \frac{e^{\hbar\omega/k_B T}}{(e^{\hbar\omega/k_B T} - 1)^2} g(\omega) d\omega \quad (2)$$

is shown in figure 7(a).

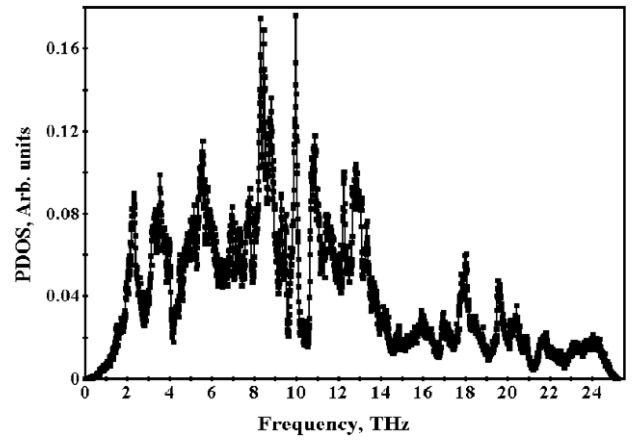


Figure 8. Phonon density of states for Mn_2GeO_4 .

The non-lattice contributions in the temperature range from T_3 to T_N , except for the narrow region near T_2 , are described as the sum of the Schottky contribution and the magnetic contribution:

$$C_v^{\text{non-latt}}(T) = C_v^{\text{Sch}}(T) + C_v^{\text{mag}}(T). \quad (3)$$

Dachs *et al* [19] demonstrated that the Schottky contribution C_v^{Sch} to the specific heat of fayalite can be determined by the expression

$$C_v^{\text{Sch}}(T) = K_1 (K_2/T)^2 \frac{\exp(K_2/T)}{1 + \exp(K_2/T)^2}. \quad (4)$$

Thus we applied equation (4) for the case of Mn-olivine.

The contribution of the magnetic phase transition to the specific heat at $T < T_N$ according [21] was simulated as

$$C_v^{\text{mag}}(T) = K_3 \ln \frac{1 + (T/T_N)^m}{1 - (T/T_N)^m}. \quad (5)$$

Coefficients K_1 , K_2 , K_3 and m were determined by fitting to the experimental data. Table 3 summarizes the fitted parameters.

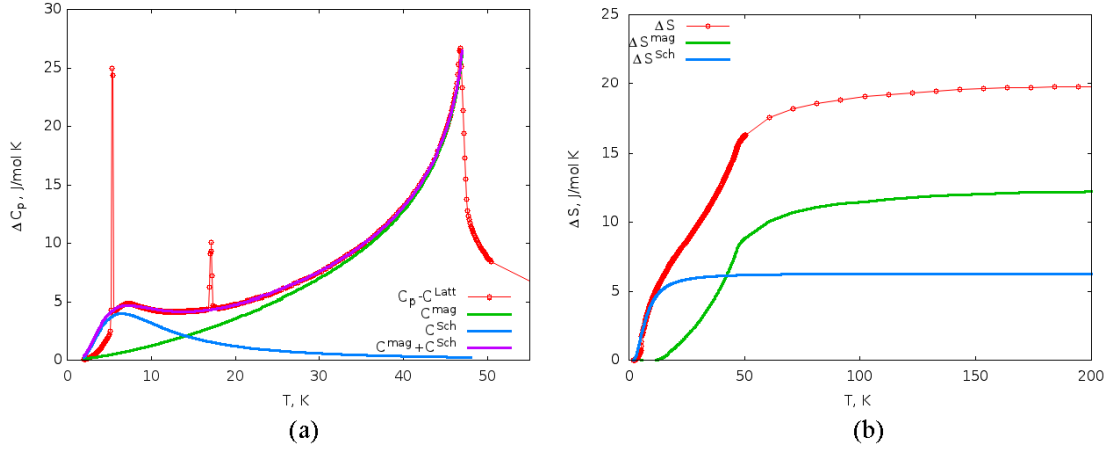


Figure 9. (a) Experimental non-lattice specific heat (open circles) with the magnetic and Schottky anomaly contributions for Mn_2GeO_4 obtained by fitting to equation (3) (solid lines). (b) Contributions to the entropy of Mn_2GeO_4 .

Table 3. Coefficients from fitting of the experimental specific heat of Mn_2GeO_4 to equation (3).

Parameter	Coefficient
K_1	$9.1 \text{ J mol}^{-1} \text{ K}^{-1}$
K_2	15.6 K
K_3	$6.3875 \text{ J mol}^{-1} \text{ K}^{-1}$
m	1.49

Once the expression for the non-lattice and the set of fitted parameters was identified, the global fitting was applied, whereby all the terms appearing in equation (3) are treated together. The results are shown in figure 9(a). Satisfactory agreement is obtained over the entire temperature range from T_3 to T_N . Note that in our Mn_2GeO_4 samples, the temperature of the Schottky anomaly maximum is lower than, for example, in Fe_2SiO_4 , since the spin-orbit coupling parameter of the Mn^{2+} ion ($\lambda \approx 60 \text{ cm}^{-1}$) differs from that of Fe^{2+} ($\lambda \approx 100 \text{ cm}^{-1}$) [17].

Now, we estimate the entropy with regard to the ordering of magnetic Mn^{2+} ions. The non-lattice contributions to the entropy (ΔS) with the magnetic (ΔS_{mag}) and Schottky (ΔS_{Sch}) entropies are presented in figure 9(b). It can be seen that the limit theoretical value of magnetic entropy $\Delta S 2R \ln 6$ ($29.79 \text{ J mol}^{-1} \text{ K}^{-1}$) is not attained. Unfortunately, the relaxation technique does not ensure correctness of the specific heat measurements near the pronounced first-order phase transitions and does not allow us to follow the entropy variations caused by the phase transitions at T_2 and T_3 . In addition, one can see that the entropy at T_N is only 70% of the limit value obtained from the experiment. It implies that the noticeable short-range order is retained by the magnetic spin systems at temperatures well above T_N and, in fact, the expected total magnetic entropy is not reached until 150 K, which is consistent with the data of the magnetic susceptibility measurements.

The value of magnetic entropy ΔS_{mag} is close to the value $R \ln 6$ ($14.8 \text{ J (mol K)}^{-1}$) instead of $2R \ln 6$ ($29.79 \text{ J mol}^{-1} \text{ K}^{-1}$). Thus, we see that not all magnetic ions are responsible for the λ -anomaly at T_N , which

confirms our assumption on the existence of two magnetic subsystems in Mn_2GeO_4 , one contributing to the λ -anomaly at T_N and the other to the Schottky one. Until now, we have not been able to answer unambiguously the question as to which of the subsystems is responsible for either anomaly. At the same time, the authors of [17] stated that in Fe_2SiO_4 the M1 subsystem appears in the specific heat as the Schottky anomaly, which explains the ‘shoulder’ in the specific heat curve near 20 K, while the M2 subsystem contributes mainly to the critical λ -anomaly. This statement is applicable also to Mn_2GeO_4 , considering the M1 subsystem to be Mn1 and the M2 subsystem to be Mn2.

Thus, the specific heat measurements showed the occurrence of three pronounced magnetic phase transitions in Mn_2GeO_4 , while in other olivines (for example, Fe_2SiO_4) there is only the λ -anomaly. All the three transitions at T_1, T_2 and T_3 correspond exactly to the magnetic phase transitions in the magnetization curve. The results of the specific heat measurements suggest that at $T_1 = T_N$ only the Mn2 subsystem is fully antiferromagnetically ordered, while the Mn1 moments cant from the c axis.

3.4. Phase diagrams

The detail analysis of the field dependences of magnetization in different directions and characteristic temperature ranges (section 3.2) appears useful for building magnetic phase diagrams.

Figures 10(a) and (b) show the magnetic phase diagrams (H_c versus T) for Mn_2GeO_4 that were built on the basis of our magnetic and specific heat data. One can see the sharp boundaries between the magnetic states: $T > T_1$ is the range of the paramagnetic phase, 1 and 3 are the antiferromagnetic phases with weak ferromagnetic moments of different origins, and 2 is the antiferromagnetic collinear phase.

The magnetic phase diagrams (figures 10(a) and (b)) reflect the main conclusions of the analysis of the field dependences of magnetization. These conclusions are briefly discussed in this section.

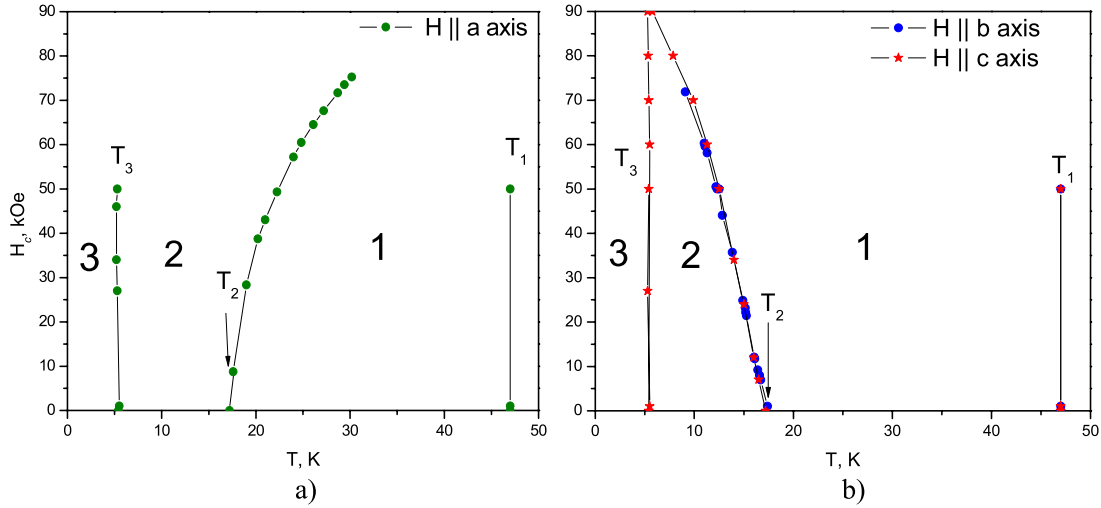


Figure 10. Magnetic phase diagrams for (a) $H \parallel$ the a axis and (b) $H \parallel$ the b, c axes built on the basis of the magnetic and specific heat data for Mn_2GeO_4 .

It can be seen in the temperature dependence of H_c for the a axis (figure 10(a)) that as the temperature is decreased, the critical field H_{ca} of the transition decreases and tends to zero at $T = 17$ K; i.e., the antiferromagnetic vector is parallel to the a axis, $L \parallel a$, at $H < H_{ca}$ in region 1. In region 2 for the b axis, critical field H_{cb} grows with decreasing temperature. In this case, vector L at $H < H_{cb}$ is parallel to the b axis. We suggest that L is reoriented in the ab plane. It is obvious that $T = 17$ K is the temperature of the spontaneous reorientation. Taking into account that at $T_2 = 17$ K along the c axis in the temperature range T_2 – T_3 , the observed weak ferromagnetic moment vanishes, we may suggest that in Mn_2GeO_4 at $T = 17$ K the Morin transition occurs [22]. The phase diagram along the c axis presented in figure 10(b) is similar to the diagram from [7].

3.5. Magnetic resonance measurement

Since the features of the crystal structure and the assumed presence of the magnetic subsystems create the prerequisites for implementation of the complex magnetic structure in Mn_2GeO_4 , we studied the resonance properties by the antiferromagnetic resonance (AFMR) method. Previously [23], we successfully used this method to study the two-subsystem CuB_2O_4 magnetic compound.

The frequency-field and temperature dependences of the resonance properties of the Mn_2GeO_4 single crystal were investigated on a magnetic resonance spectrometer in the frequency range 25–140 GHz in pulsed magnetic fields up to 80 kOe. The detailed analysis of the resonance properties of this crystal will be published later. Here, we present some characteristic results.

The frequency-field dependences of the resonance measured at $T = 4.2$ K in a magnetic field along the rhombic a and b axes are presented in figure 11.

In the a axis direction, the frequency-field dependence is typical of an antiferromagnet and described by the

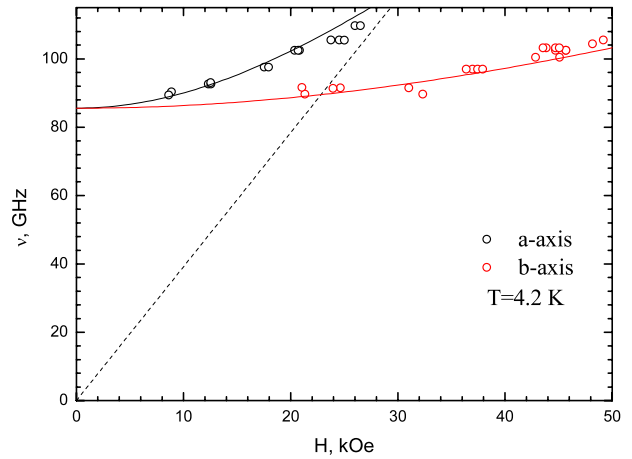


Figure 11. AFMR frequency–field dependences in magnetic fields along the a and b axes at $T = 4.2$ K.

relation [24]

$$\left(\frac{\omega}{\gamma}\right)^2 = H^2 + H_{\Delta}^2, \quad (6)$$

where $\gamma H_{\Delta} = \gamma \sqrt{2H_E H_a} = \omega_c$ —energy gap of the AFMR spectrum.

As the external magnetic field H is increased, the frequency of this branch tends to the linear dependence $\omega = \gamma H$ (dashed line in the figure).

If the field is directed along the b axis, the frequency–field dependence is flat and intersects the dependence $\omega = \gamma H$. Such flat dependences are characteristic of magnets with a spiral magnetic structure. Similar flat dependences were reported in [25, 26]. The experimental data for the b axis in the figure are described well by the equation

$$\omega = \sqrt{\omega_c^2 + kH^2} \quad (7)$$

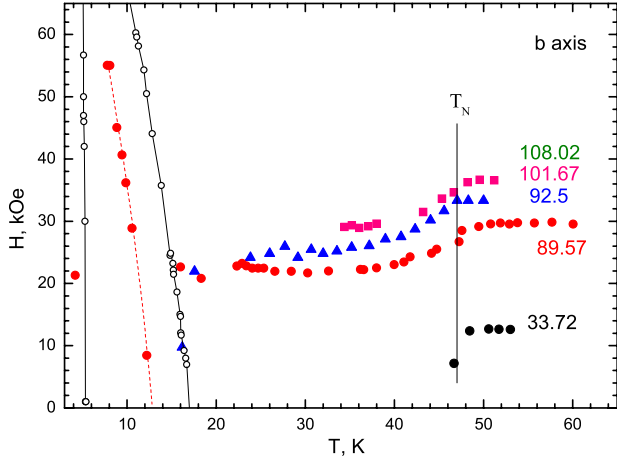


Figure 12. Temperature dependences of the resonance fields at different frequencies for magnetic fields oriented along the *b* direction.

with the parameters $\omega_c = 85.57$ GHz and $k = 0.16$ GHz² kOe⁻².

The above value of the energy gap was fitted simultaneously for the resonance data measured along the *a* and *b* axes. The theoretical dependences built using equations (6) and (7) for these parameters are presented in the figure by solid lines.

The absence of features in the frequency–field dependence for the *a* axis under the assumption of the spiral structure can be explained by the fact that the spiral plane, according to [7], is perpendicular to this axis and at this orientation of the field the spiral character of the magnetic structure is not felt. At the same time, for the *c* axis, as well as for the *b* axis, the frequency–field dependence should also be flat and weakly dependent on a magnetic field. However, we did not find resonance absorption for this direction at $T = 4.2$ K in the accessible frequency range 25–140 GHz. It is apparently related to the fact that the Mn₂GeO₄ crystal belongs to the orthorhombic syngony. The antiferromagnetic resonance spectrum of such antiferromagnets contains two resonance branches with different initial splittings [25, 27]. The initial splitting for this direction is apparently above 140 GHz and therefore not observed at the helium temperature. Using the dependence $\omega_c(T)$ that was obtained along the *c* axis and is described well by the Brillouin function, we estimated the splitting $\omega_c(0) = 151$ GHz.

Let us consider the temperature dependence of the resonance field for the external magnetic field oriented along the *b* axis (figure 12). The temperature dependence at a frequency of 89.57 GHz, for which the absorption was detected at temperatures from 4.2 to 60 K, can be divided into four portions in accordance with the regions in the phase diagram (figure 10(b)) whose boundaries are shown in the figure by black lines (open circles). In each region of the phase diagram, there are continuous monotonic dependences drastically changing at the transition through the phase boundary. In the low-temperature region, the resonance absorption was observed only at $T = 4.2$ K. The

Table 4. Interatomic distances and angles in Mn₂GeO₄ corresponding to the indirect magnetic exchange interactions (based on our single-crystal x-ray diffraction measurements).

	λ (Å)	θ (deg)	
Mn1–Mn1			
Mn1 ¹ –O1, Mn1 ² –O1	2.185	Mn1 ¹ –O1–Mn1 ²	92.47
Mn1 ¹ –O3, Mn1 ² –O3	2.198	Mn1 ¹ –O3–Mn1 ²	91.78
Mn1–Mn2			
Mn1 ¹ –O1, Mn2 ² –O1	2.185 2.266	Mn1–O1–Mn2 ²	99.2
Mn1 ¹ –O2, Mn2 ¹ –O2	2.269 2.350	Mn1 ¹ –O2–Mn2 ¹	94.41
Mn1 ¹ –O3, Mn2 ⁴ –O3	2.198 2.144	Mn1 ¹ –O3–Mn2 ⁴	124.7
Mn1 ¹ –O2, Mn2 ³ –O2	2.269 2.159	Mn1 ¹ –O3–Mn2 ³	117.3
Mn2–Mn2			
Mn2 ³ –O2, Mn2 ¹ –O2	2.159 2.350	Mn2 ³ –O2–Mn2 ¹	130.7

experimental value of the resonance field at this temperature corresponds to the frequency–field dependence for the *b* axis in figure 11. At the transition to the intermediate region of the phase diagram, the resonance field grows stepwise and then sharply decreases with a further increase in temperature. Temperature dependences of the resonance fields for higher frequencies are similar to the dependence for 89.57 GHz and located below the latter (the higher the frequency, the lower the dependence is located). Thus, in this region of the phase diagram the frequency–field dependence drops; i.e., the resonance frequency at a fixed temperature decreases as the field is increased. Such dependences are usually observed for antiferromagnets when the magnetic field is directed along the antiferromagnetic axis. Thus, the dropping frequency–field dependence may imply that in this intermediate state the magnetic moments of the antiferromagnetic sublattices are directed along the rhombic *b* axis.

At the transition to the high-temperature ordered phase, the resonance field jumps again and with a further increase in temperature the values of the resonance field for all frequencies rises smoothly, tending to the values characteristic of the paramagnetic state and determined by the equation $\omega = \gamma H$ on approaching the Neel temperature. In this temperature range, the frequency–field dependence for the *b* direction has the typical form (6); in this case, the resonance field grows because the energy gap ω_c tends to zero on approaching T_N . In the paramagnetic region, the resonance field is independent of temperature.

Thus, the AFMR data confirm the results of the magnetic measurements (figure 10) and refine the magnetic state of the crystal at the transition through the boundaries of the

Table 5. Exchange interactions in Mn₂GeO₄.

J_{ij} (K)	\uparrow Mn1 ¹	\downarrow Mn1 ²	\uparrow Mn1 ³	\downarrow Mn1 ⁴	\uparrow Mn2 ¹	\downarrow Mn2 ²	\downarrow Mn2 ³	\uparrow Mn2 ⁴
\uparrow Mn1 ¹	0	-10.6(2)	0	0	-5.3	-5.3	-3.9	-3.9
\downarrow Mn1 ²	-10.6(2)	0	0	0	-5.3	-5.3	-3.9	-3.9
\uparrow Mn1 ³	0	0	0	-10.6(2)	-3.9	-3.9	-5.3	-5.3
\downarrow Mn1 ⁴	0	0	-10.6(2)	0	-3.9	-3.9	-5.3	-5.3
\uparrow Mn2 ¹	-5.3	-5.3	-3.9	-3.9	0	0	-10(4)	0
\downarrow Mn2 ²	-5.3	-5.3	-3.9	-3.9	0	0	0	-10(4)
\downarrow Mn2 ³	-3.9	-3.9	-5.3	-5.3	-10(4)	0	0	0
\uparrow Mn2 ⁴	-3.9	-3.9	-5.3	-5.3	0	-10(4)	0	0

magnetic phase diagram. It was determined that below 5.5 K the magnetic spiral structure can be implemented, which is consistent with the data reported in [7]. Unfortunately, at this stage of investigations we failed to observe the resonance absorption, confirming the presence of magnetic subsystems, by the AFMR method. We are planning to continue these works in broadened field and frequency ranges.

3.6. Estimation of the exchange interactions in Mn₂GeO₄

The effect of two magnetic subsystems on the complex magnetic structure of the investigated compound can be assumed not only based on the anomalous temperature dependence of magnetic entropy in Mn₂GeO₄ (figure 9(b)), but also by estimating exchange interactions in Mn₂GeO₄.

Since in Mn₂GeO₄ all the Mn–Mn distances are much longer than the distances between manganese and oxygen, the direct Mn–Mn exchange interactions can be neglected. The main role is played by the indirect exchange interactions between two manganese ions via one bridge oxygen ion. The total number of Mn–O–Mn paths is 12 for both Mn1 and Mn2 cations. All the exchange paths are described by seven indirect magnetic interactions (figure 13) via oxygen anions.

Table 4 gives interatomic distances and angles in Mn₂GeO₄ that correspond to the main indirect couplings responsible for the exchange interactions both inside the Mn1 and Mn2 subsystems and between them.

It can be seen that all the angles can be combined into two groups: 90°–100° and 100°–130°. For these groups, we write two integrals of the exchange interactions using a simple model for their calculation [28, 29]:

$$\begin{aligned}
 J_1 &= -\frac{4}{75}c(8b + 3c)U, & (\sim 90^\circ) \\
 J_2 &= -\frac{4}{25}\left(\frac{8}{9}b^2 + c^2\right)U|\cos\theta|, & (\sim 180^\circ,).
 \end{aligned}
 \tag{8}$$

Here, b and c are the parameters of the electron transport ligand–cation by the σ and π couplings, respectively, θ is the indirect coupling angle and U is the energy of the ligand–cation electron excitation. Taking the values typical

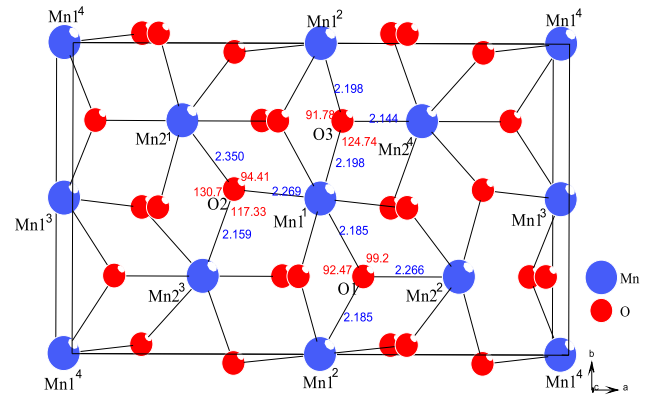


Figure 13. A part of the Mn₂GeO₄ crystal unit cell showing different exchange paths between Mn ions via O. Superscripts ^{1,2,3,4} mark the numbers of magnetic sublattices.

for oxides $b = 0.02$, $c = 0.01$ and $U(\text{Mn}) = 4.5$ eV [29], we obtain $J_1 \approx -5.3$ K and $J_2 \approx -1.7$ K for $\theta = 117.3^\circ$, $J_2 \approx -2.2$ K for $\theta = 124.7^\circ$ and $J_2 \approx -2.5$ K for $\theta = 130.7^\circ$ (for convenience, the final values of the exchange integrals are given in kelvin), where minus means that all the interactions are antiferromagnetic, unlike the data reported in [7] where the authors suggested the ferromagnetic exchange in the ab plane. By summation of the exchange interactions with regard to the number of nearest neighbors in a unit cell, we obtain the values given in table 5. Arrows indicate the mutual orientations of the magnetic moments of the sublattices.

The values given in bold characterize the exchange interactions participating in the establishment of the magnetic order in each subsystem and the italicized values are the competing inter-subsystem Mn1–Mn2 interactions. It can be seen that each chain Mn1 cation can both enhance and weaken the contribution to the interaction with plane Mn2 cations and these contributions are mutually compensated. In this case, we have two independent magnetic subsystems: chain Mn1 and plane Mn2. The interaction between Mn1 and Mn2 in the ab plane can be illustrated as the interaction of triangular configurations (figure 1(b)), which indicates the geometrical

frustration [30]. Despite this circumstance and the negative values of all the exchange interactions, we cannot draw an unambiguous conclusion that Mn_2GeO_4 is the magnetic system with the strong frustration, taking into account that the relation $f = |\Theta_{\text{CW}}|/T_{\text{N}} > 10$ typical of the strong frustration does not work here. We can merely speak about individual frustrated regions, which apparently play a certain role in the formation of the complex magnetic structure of Mn_2GeO_4 .

4. Conclusions

For the first time, high-quality Mn_2GeO_4 single crystals have been grown by the flux method. The magnetic, resonance and thermodynamic properties of the single crystals have been investigated. The presence of several magnetic phases has been established: the high-temperature phase at $T_2 < T < 47.7$ K, with T_2 being dependent on an applied magnetic field, the intermediate phase at $5.5 \text{ K} < T < T_2$, and the low-temperature phase at $T < 5.5$ K. At the current stage of investigations, the antiferromagnetic state with a weak ferromagnetic moment in the high-temperature phase and the incommensurate phase below 5.5 K have been determined. The magnetic structure of the intermediate phase still remains unclear. The effect of two magnetic subsystems on the complexity of the magnetic structure and phase diagrams is a subject for further investigations.

Acknowledgments

This study was supported by the Siberian Branch of the Russian Academy of Sciences, integration project no. 29 and project no. 2.5.2. Also we thank Dr Viktor Zinenko and Dr Sergey Martynov for useful discussions.

References

- [1] Toropov N A, Barzakovskii P B, Lapin V V and Kurtseva N N 1965 *State Diagrams of the Silicate Systems* (Moscow: Nauka)
- [2] Saponova N V, Volkov N V, Sablina K A, Petrakovskii G A, Bayukov O A, Vorotynov A M, Velikanov D N, Bovina A F, Vasil'ev A D and Bondarenko G V 2009 *Phys. Status Solidi b* **246** 206
- [3] Balaev A D, Volkov N V, Saponova N V, Sablina K A and Vasil'ev A D 2009 *J. Phys.: Condens. Matter* **21** 336006
- [4] Jodlauk S, Becker P, Mydosh J A, Khomskii D, Lorenz T, Streltsov S V, Hezel D C and Bohat'y L 2007 *J. Phys.: Condens. Matter* **19** 432201
- [5] Redhammer G J, Roth G, Treutmann W, Hoelzel M, Paulus W, Andre G, Pietzonka C and Amthauer G 2009 *J. Solid State Chem.* **182** 2374
- [6] Petrakovskii G A, Popov M A, Balaev A D, Sablina K A, Baykov O A, Velikanov D A, Vorotynov A M, Bovina A F, Vasil'ev A D and Boehm M 2009 *Phys. Solid State* **51** 1853
- [7] White J S, Honda T, Kimura K, Kimura T, Niedermayer Ch, Zaharko O, Poole A, Roessli B and Kenzelmann M 2012 *Phys. Rev. Lett.* **108** 077204
- [8] Volkov N V, Balaev A D, Saponova N V, Sablina K A, Velikanov D A, Molochev M S and Popkov S I 2011 *Abstract Book: Moscow Int. Conf. on Magnetism* p 184
- [9] Sheldrick G M 1990 *Acta Crystallogr. A* **46** 467
- [10] Tugarinov V I, Makievskii I Y and Pankrats A I 2004 *Instrum. Exp. Tech.* **47** 472
- [11] Creer J G and Troup G J F 1970 *Solid State Commun.* **8** 1183
- [12] Ballet O, Fuess H, Wacker K, Untersteller E, Treutmann W, Hellner E and Hosoya S 1989 *J. Phys.: Condens. Matter* **1** 4955
- [13] Sazonov A, Meven M, Hutanu V, Heger G, Hansen T and Gukasov A 2009 *Acta Crystallogr. B* **65** 664
- [14] Pankrats A I, Petrakovskii G A, Bezmaternykh L N and Temerov V L 2008 *Phys. Solid State* **50** 79
- [15] Pankrats A, Petrakovskii G, Kartashev A, Eremin E and Temerov V 2009 *J. Phys.: Condens. Matter* **21** 436001
- [16] Robie R A, Hemingway B S and Takei H 1982 *Am. Mineral.* **67** 470
- [17] Aronson M C, Stixrude L, Davis M K, Gannon W and Ahilan K 2007 *Am. Mineral.* **92** 481
- [18] Woodfield B F, Boerio-Goates J, Shapiro J L, Putnam R L and Navrotsky A 1999 *J. Chem. Thermodyn.* **31** 245
- [19] Dachs E, Geiger C A, von Seckendorff V and Grodzicki M 2007 *J. Chem. Thermodyn.* **39** 906
- [20] Pavlovskii M private communication
- [21] Inden G 1981 *Physica B + C* **103** 82
- [22] Morin F 1950 *J. Phys. Rev.* **78** 819
- [23] Boehm M, Roessli B, Schefer J, Wills A S, Staub U and Petrakovskii G A 2003 *Phys. Rev. B* **68** 024405
- [24] Nagamiya T, Yosida K and Kubo R 1955 *Adv. Phys.* **4** 1
- [25] Kimura S, Hagiwara M, Ueda H, Narumi Y, Kindo K, Yashiro H, Kashiwagi T and Takagi H 2006 *Phys. Rev. Lett.* **97** 257202
- [26] Vorotynov A et al 1998 *JETP* **86** 1020
- [27] Glazkov V N, Smirnov A I, Petrenko O A, Paul D M K, Vetkin A G and Eremina R M 1998 *J. Phys.: Condens. Matter* **10** 7879
- [28] Anderson P W 1959 *Phys. Rev.* **115** 1
- [29] Bayukov O A and Savitskii A F 1989 *Phys. Status Solidi b* **155** 249
- [30] Hagemann I S and Khalifah P G 2000 *Phys. Rev.* **62** R771